



3D simulation of short fatigue crack propagation by finite element crystal plasticity and remeshing



H. Proudhon^{a,*}, J. Li^a, F. Wang^a, A. Roos^b, V. Chiaruttini^b, S. Forest^a

^a MINES ParisTech, PSL Research University, MAT – Centre des matériaux, CNRS UMR 7633, BP 87, 91003 Evry, France

^b ONERA, The French Aerospace Lab, Châtillon, France

ARTICLE INFO

Article history:

Received 3 November 2014

Received in revised form 13 May 2015

Accepted 26 May 2015

Available online 15 June 2015

Keywords:

Crystal plasticity

Finite element

Short fatigue crack propagation

Adaptive remeshing

ABSTRACT

An iterative method to simulate 3D fatigue crack propagation in crystalline materials is proposed and demonstrated on simple test cases. The method relies on the computation of a damage indicator based on plastic activity around the crack tip. By post-processing this quantity after a given loading sequence, local crack direction and growth rate are estimated along the crack path. Dedicated remeshing routines allow the crack to propagate in 3D and the iterative process can continue with the updated crack geometry. Two examples in a BCC single crystal featuring different slip systems demonstrate the crack propagation simulations under cyclic loading over distances comparable to the crystal size and with non-regular crack shapes such as zig-zag crack paths. The effect of transferring plastic fields between propagation steps is also analysed.

© 2015 Elsevier Ltd. All rights reserved.

1. Introduction

In many cases, the first stages of fatigue crack propagation in metallic polycrystalline materials under low loading amplitudes are very sensitive to microstructural features. These are called microstructurally small cracks. Several mechanisms based on local slip activity at the crack tip for small fatigue crack propagation were proposed in the past [1–3]. A double slip mechanism was introduced by Neumann that described an alternating crack propagation along two slip planes [4]. This zigzag crack growth has been confirmed experimentally in many FCC single crystals and polycrystals by surface observations [5,6]. Since then, X-ray tomography has steadily developed and can now be used to study complex 3D crack paths [7–10]. In addition, with the substantial progress in the microstructural characterisation techniques, it is now possible to observe small fatigue cracks together with the surrounding 3D grain microstructure. The fracture surface of small fatigue cracks is a complex combination of slip planes which changes from one grain to another, as characterised by Herbig et al. [11] using synchrotron X-ray tomography coupled with diffraction contrast tomography [12]. In addition to the complex crack paths, the crack growth rate is influenced by grain boundaries, as observed by Schaefer et al. using FIB tomography [13].

In the 1980s, the first crystal plasticity models were implemented by Asaro [14] and applied to simulations of fatigue loading using the notions of shear stress and slip deformation. A phenomenological model was proposed by Méric et al. [15], in which slip systems and crystallographic orientations of the grains are taken into account as the material parameters. This model can simulate the slip localisation at the crack tip as predicted by Rice [16]. It was later used to simulate fatigue crack propagation based on continuum damage mechanics [17].

Simulation techniques of microstructurally small cracks have improved steadily through the last 10 years [18] although it is still a very difficult problem from a numerical point of view. The details of the crack growth mechanisms and grain boundary crossing are still under debate. Discrete dislocation simulations can bring some insight on simplified configurations [19,20] but a physically based criterion capable of simulating short fatigue crack growth in a polycrystalline microstructure has not yet emerged. In that sense, the direct comparison of numerical simulations with experiments is very promising. In this work, a new numerical method is developed to simulate the complex small fatigue crack path, with the local approach to fracture coupled with Crystal Plasticity Finite Element (CPFE) simulations.

2. Methodology

The methodology proposed in this work can be summarised as follow, see also Fig. 1. From CPFE computations of a cracked body

* Corresponding author.

E-mail address: henry.proudhon@mines-paristech.fr (H. Proudhon).

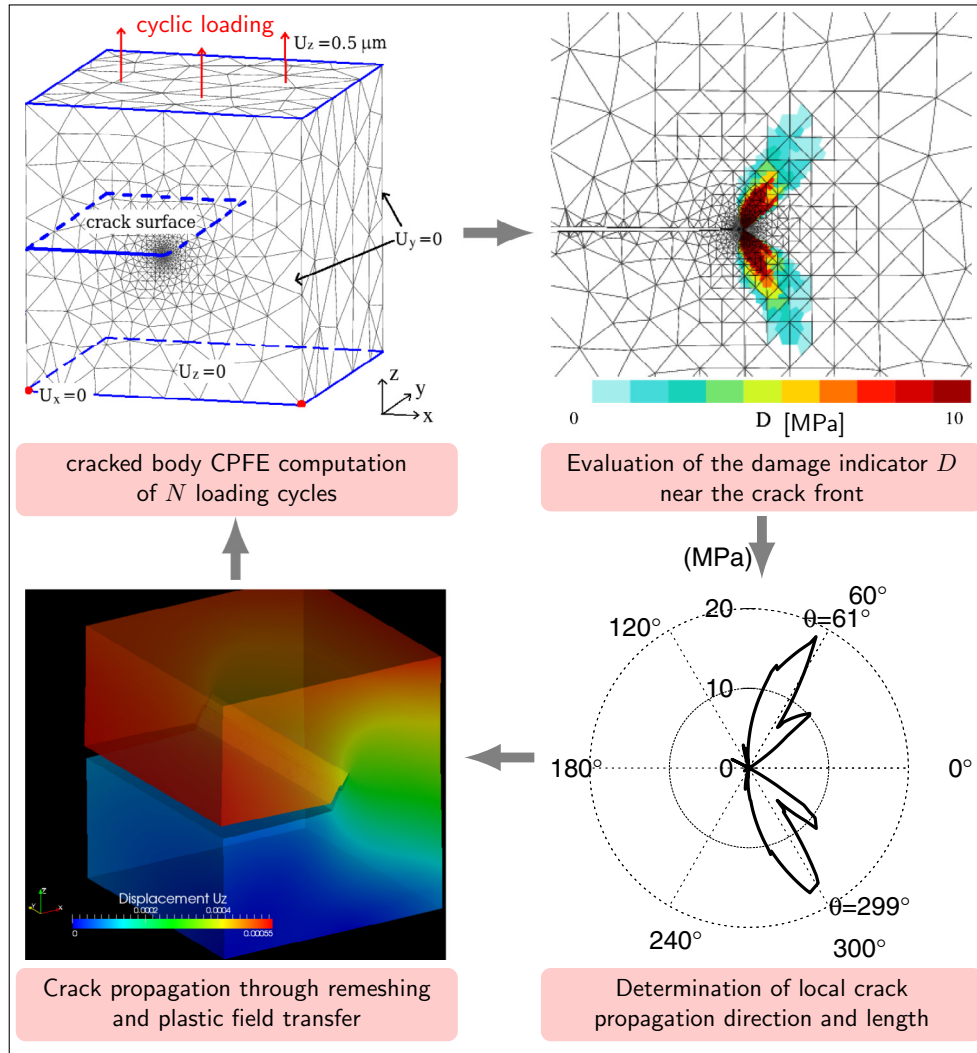


Fig. 1. Principle of the proposed iterative crack propagation simulation methodology.

(Fig. 1a), a damage indicator based on the accumulated slip, the resolved shear stress and the normal stress on each slip system are calculated at each integration point and for every time increment (Fig. 1b). The crack growth direction is then determined by analysing this damage indicator in the region around the crack front (Fig. 1c). The crack is extended via remeshing at each propagation event (Fig. 1d). At this point the state variables can be transferred to the new mesh corresponding to the new crack configuration. The CPFE computation is then continued. Each step of the crack growth simulation methodology is explained in full detail in the next paragraphs.

2.1. Crystal plasticity model

In order to analyse the slip system activity and to determine the driving force for short crack propagation, an elasto-visco-plastic crystal plasticity model was selected [15]. The CPFE computations were carried out in the framework of infinitesimal strains using the Z-set software [21], because in the experiments only small deformations were observed at the crack front.

The total strain tensor $\tilde{\varepsilon}$ is partitioned into an elastic part $\tilde{\varepsilon}^e$ and a plastic part $\tilde{\varepsilon}^p$. To concentrate on the effect of the plastic activity on the crack growth, the material is considered linear and isotropic

regarding elasticity. Depending on the material, the elastic anisotropy may play an important role on the global stress equilibrium and change the results. Here, according to Hooke's law:

$$\tilde{\varepsilon} = \frac{1+\nu}{E} \tilde{\sigma} - \frac{\nu}{E} \text{tr}(\tilde{\sigma}) \mathbf{1}, \quad (1)$$

with $\mathbf{1}$ the second-order identity tensor, the Young's modulus $E = 110$ GPa and the Poisson's ratio $\nu = 0.3$.

The plastic strain is the result of S potentially active slip systems. For instance, octahedral slip in FCC crystals can occur in 12 different $(111)\langle 110 \rangle$ systems, while slip in BCC material can mainly occur in a combination of 12 $(110)\langle 111 \rangle$, 12 $(112)\langle 111 \rangle$ and 24 $(123)\langle 111 \rangle$. Here, for simplicity, simplified cases will be considered with only one slip system in Section 3.2 and 2 slip systems in Section 4. The plastic strain rate is calculated according to

$$\dot{\tilde{\varepsilon}}^p = \sum_{s=1}^S \dot{\gamma}^s \tilde{\mathbf{m}}^s, \quad (2)$$

where $\tilde{\mathbf{m}}^s$ is the orientation tensor defined by the slip plane normal $\tilde{\mathbf{n}}^s$ and the slip direction $\tilde{\mathbf{f}}^s$ of each system s , and $\dot{\gamma}^s$ is the slip rate defined by a power law:

$$\tilde{\mathbf{m}}^s = \frac{1}{2} (\tilde{\mathbf{n}}^s \otimes \tilde{\mathbf{f}}^s + \tilde{\mathbf{f}}^s \otimes \tilde{\mathbf{n}}^s), \quad (3)$$

$$\dot{\gamma}^s = \text{sign}(\tau^s) \left\langle \frac{|\tau^s| - \tau_0}{K} \right\rangle^n, \quad (4)$$

with parameters $K = 300 \text{ MPa s}^{1/n}$ and $n = 3$. The critical resolved shear stress $\tau_0 = 300 \text{ MPa}$ and $\tau^s = \sigma : \mathbf{m}^s$ is the shear stress resolved on slip system s . Here again for simplicity no hardening is introduced in the material model used throughout this paper.

2.2. Fatigue damage indicator

Crack initiation is not studied here and the presence of an initial defect in the structure is assumed. Its location and size may be predicted by suitable crack initiation models ranging from multi-axial fatigue criteria to calculations using a continuum damage model. Throughout this paper, an artificial crack perpendicular to the loading direction but not coincident with a slip plane will be used, see Fig. 1a. This is inspired by the small notches used in past experiments to control the crack initiation location as in [13,11].

During cyclic loading of the pre-cracked sample, plastic deformation occurs near the crack tip due to the dislocation movements along the slip planes. This mechanism is described by the slip γ^s on each slip system s in the crystal plasticity model. It is governed by mode II loading and driven by the resolved shear stress τ^s , as explained in [22]. In addition, it was demonstrated that the normal stresses σ_n^s acting on the slip planes may also influence nucleation and short crack propagation [23]. Therefore, in this work a damage indicator that is the combination of γ^s , τ^s and σ_n^s is retained. Previously, similar forms were proposed by Fatemi et al. [23–25]. Here, at each integration point the damage indicator D at time t is the maximum value among the slip systems s , according to

$$D(t) = \max_s \int_0^t |\dot{\gamma}^s| (|\tau^s| + k(\sigma_n^s)) dt, \quad (5)$$

with k a material parameter controlling the sensitivity of the crack propagation to the normal stress on the slip plane s . The parameter k was set to 0.4 [23]. Via the operator $\langle \cdot \rangle$, only the positive part of the normal stress is taken into account to assist the crack propagation. Fig. 1b shows an example of the damage indicator.

2.3. Crack growth direction and distance by post-processing the damage indicator

During the numerical procedure, an approximated smoothed crack front Γ , composed of $i + 1$ equidistant control points P_k ($0 \leq k \leq i$) on the initial crack front, is computed [26]. For each point, a local orthonormal coordinate basis $(\hat{\mathbf{B}}_k, \hat{\mathbf{T}}_k, \hat{\mathbf{N}}_k)$ associated to P_k is computed, $\hat{\mathbf{B}}_k$, $\hat{\mathbf{T}}_k$ and $\hat{\mathbf{N}}_k$ locally normal to the crack front, tangent to the crack front and normal to the crack plane, respectively.

The damage indicator $D(t)$ is computed during the CPFÉ calculation at all integration points. At the end of the N cycles loading sequence, the propagation angle θ is determined by post-processing the radial distributions of D at each control point P_k of the curve representing the crack front in the plane $(\hat{\mathbf{B}}_k, P_k, \hat{\mathbf{N}}_k)$ which is locally normal to the crack. Then, the crack growth direction is selected as pointing from the origin P_k to the location where the damage indicator is the maximum, at a preset distance R_0 from the origin. The set of propagation directions along the front is used to create the geometry of the crack propagation area, which is then inserted into the FE mesh of the single crystal, as will be explained in detail in Section 2.4.

The key point here is to be able to simulate accurately the plastic activity and mechanical equilibrium at the crack tip in a small amount of fatigue cycles (here a loading sequence of N cycles) and use this result to propagate the crack over a distance representative of a much larger number of cycles (but small enough so that the crack geometry remains representative).

At each control point k the growth distance can be evaluated from the distribution of D along the crack growth direction θ_k , which decreases rapidly when moving away from the crack tip, see Fig. 2b. It is thus possible to define a threshold D_c (in MPa unit according to Eq. (5)) to define the crack growth distance d_k locally. For instance in the case of Fig. 2b, $D_c = 20 \text{ MPa}$ would give a propagation distance of $2.3 \mu\text{m}$. The critical value D_c may appear as a link between macroscopic fatigue parameters and the microscopic growth mechanisms.

For the sake of simplicity, in the two examples developed in this paper, the crack growth distance is set to a fixed value equal to R_0 . In the present case this distance corresponds to a typical value after 1000 cycles. The parameter R_0 is related to material properties, loading amplitude and other experimental conditions. The constant growth rate will introduce some oversimplification in the 3D crack growth but appears convenient to demonstrate the numerical methods. Nonetheless the numerical aspect of methodology, which is the subject of the present paper, is not fundamentally changed when using a critical value D_c instead of a fixed propagation distance.

2.4. Propagation through remeshing

All the couples $(\theta_k, d_k)_{0 \leq k \leq i}$, with $d_k = R_0$ in the case of the fixed propagation distance, define a set of $i + 1$ vectors from which a new crack front is generated. The surface of the crack extension is built using the initial and the new crack fronts. The 3D crack propagation is obtained by inserting the crack extension surface into the single crystal mesh with the Z-cracks software. Detailed information about the crack surface extension procedure is described in [26]. The state variable of the crystal plasticity model carried by the integration points of the initial mesh may be transferred to the new mesh at this stage, see Section 2.5. Next, a new CPFÉ computation is started with the new FE mesh containing the updated crack geometry. Then, the whole routine as shown in Fig. 1 is carried out again.

2.5. Field transfer of state variables

After a crack propagation event, the state variables can be transferred to the new mesh and treated as the initial state of the next CPFÉ computation [27]. The variables U^n at the node whose coordinates are \mathbf{x}_n in the new mesh are calculated using the standard FE interpolation functions P_i^o associated to the elements E^o as

$$U^n = \sum_{i \in E^o} P_i^o(\mathbf{x}_n) U_i^o, \quad (6)$$

with U_i^o the value of the nodal variables at node i of the element E^o in the initial mesh. Special attention is paid to the nodes at the crack surface because in the undeformed state, the upper and lower sides of the crack are coinciding. Variables at integration points are transferred to the new mesh using a nearest neighbour algorithm. Finally, after transferring the state variables from the old to the new mesh, the system is not in mechanical equilibrium anymore, because the previous converged state was valid only for the old mesh. However, if the errors committed by the field transfer algorithm are sufficiently small, mechanical equilibrium can be established again using a very small time increment.

3. Crack propagation in the case of a single slip system

3.1. Finite element mesh, crystal orientation and boundary conditions

In this section, the computational crack propagation method is demonstrated on a simplified test case. It consists of a $100 \mu\text{m}^3$

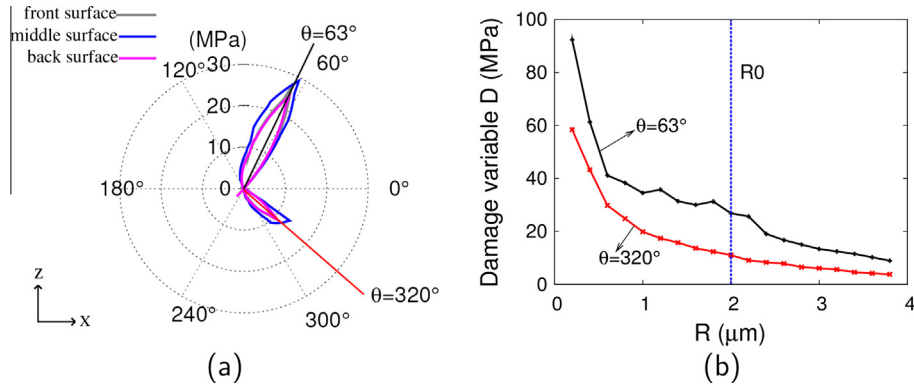


Fig. 2. (a) The damage indicator D at the end of the first loading sequence around the crack tip on the xz plane interpolated to the circles of interest of radius of $2 \mu\text{m}$ on different depths below the surface (represented by different colours). (b) The value of D at the end of the first loading sequence along two directions at $\theta = 63^\circ$ and $\theta = 320^\circ$ at the front surface. (For interpretation of the references to colour in this figure legend, the reader is referred to the web version of this article.)

single crystal with only one slip system $(112)[11\bar{1}]$. The crystal contains an initial crack perpendicular to the loading direction and the slip plane is oriented at an angle of 54.7° with respect to the crack plane, see Fig. 3. With this configuration, the initial crack plane is perpendicular to U_z (the loading axis) and the crack front is parallel to U_y which is also parallel to the crystal direction $[\bar{1}10]$. The maximum loading applied in the simulations corresponds to a nominal stress of 550 MPa.

Regarding the boundary conditions (see Fig. 1a), a displacement of $U_z = 0.5 \mu\text{m}$ is applied cyclically ($N = 5$) between 0 and the maximum value. The loading rate $\dot{\epsilon}_{zz} = 5 \times 10^{-3} \text{ s}^{-1}$ along the vertical tensile direction z , and vertical displacements are blocked at the bottom surface. Symmetry conditions in the y direction are applied at the back and the front surfaces to minimise the effect of the free surface. In this simplified case, 5 cycles are computed at each step before analysing the plastic activity through the distribution of the indicator D .

The mesh sensitivity is analysed with quadratic elements in order to find a reasonable element size with respect to the crack

growth distance R_0 . For the first crack propagation event in the single slip crystal, the analysed element sizes near the crack front are $0.1 \mu\text{m}$, $0.4 \mu\text{m}$, $0.6 \mu\text{m}$ and $0.8 \mu\text{m}$. The interpolated variables along the circles and the crack growth direction were found to be identical for every simulation except for the element size of $0.8 \mu\text{m}$ where D decreases to 23 MPa compared to 27 MPa for the element size of $0.6 \mu\text{m}$ and θ increases to 70° compared to 63° . The best compromise between numerical errors and computational time was thus to set the element size to $0.6 \mu\text{m}$ at the crack front.

3.2. Propagation results

Fig. 2a shows the evolution of D after the first loading sequence along the circles of interest at different depths along the crack front, which lies along the y -axis. The different depths are represented by different colours. The crack tip is at the centre of the figure. Two branches of D appear, respectively at $\theta = 63^\circ$ and $\theta = 320^\circ$, corresponding within 10° to the slip (parallel to the slip

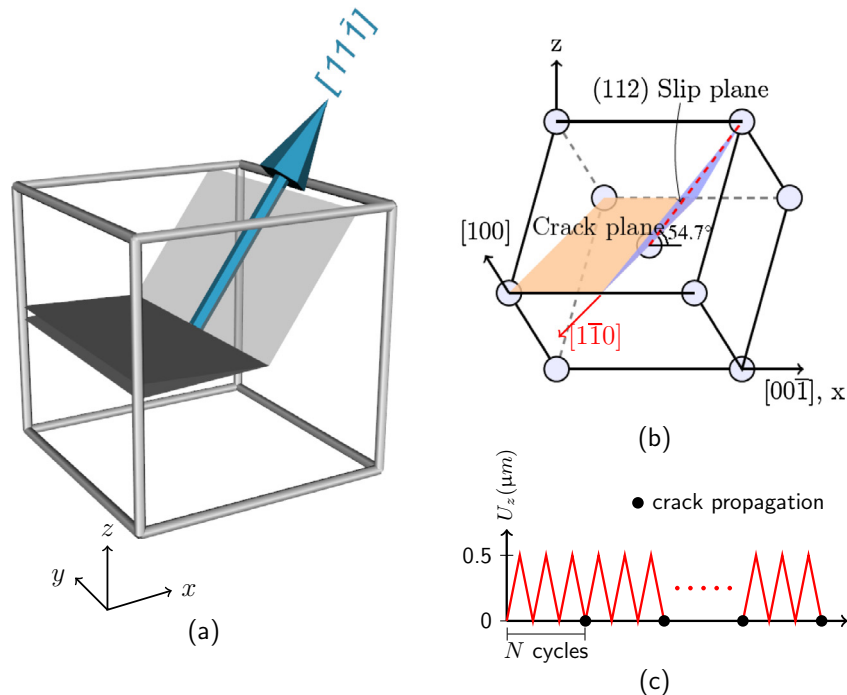


Fig. 3. (a) Schematic representation of the pre-cracked single crystal of size $100 \mu\text{m}^3$ with its slip system, (b) crystal lattice orientation and the single slip system $[11\bar{1}](112)$ of the example in the present section, and (c) global loading sequence showing crack propagation events after each series of N cycles.

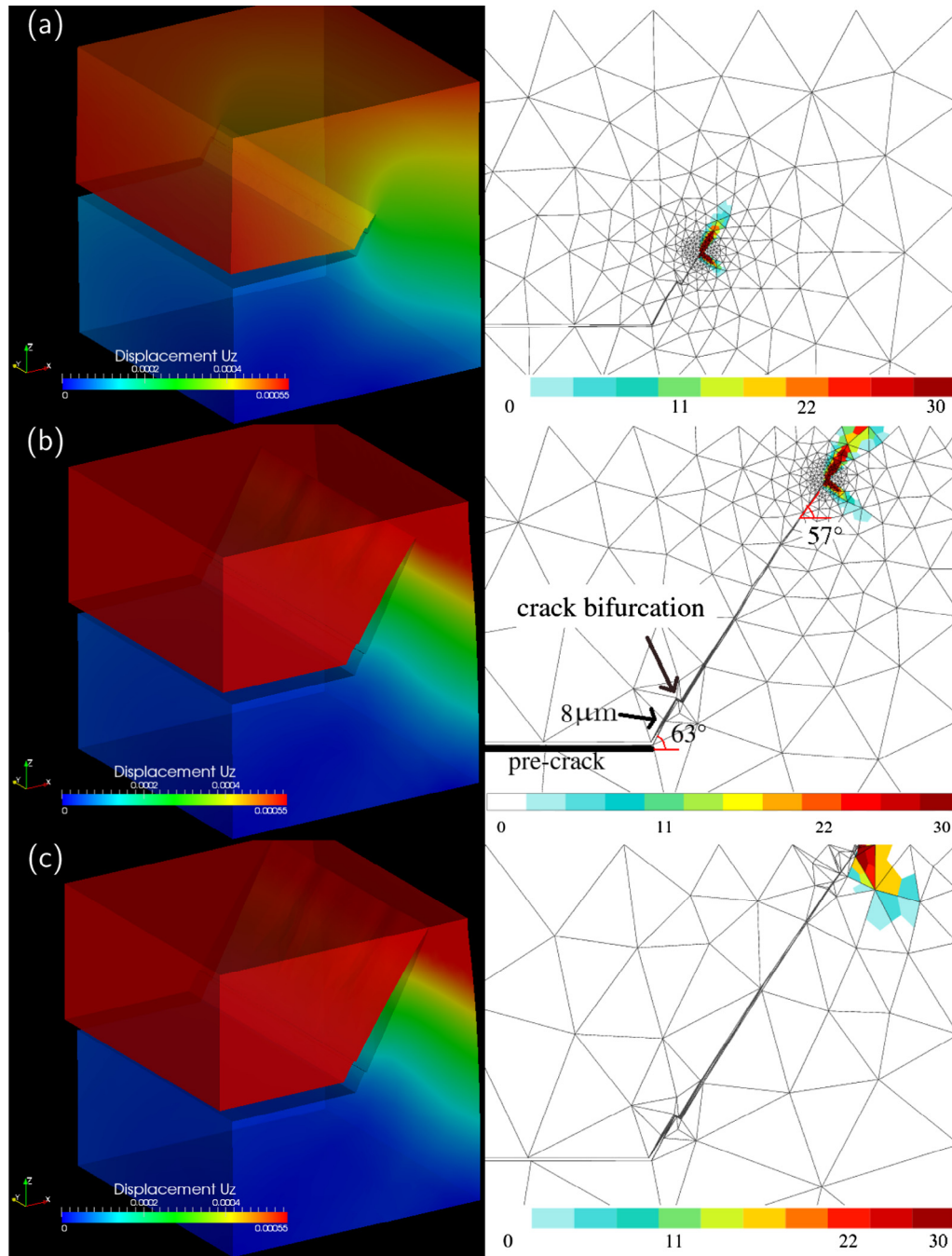


Fig. 4. Crack propagation steps in a single crystal with a single slip system showing both the displacement field in the tensile direction (in mm, the mesh deformation is magnified by a factor 10 for better visualisation) and the damage indicator D (in MPa). (a) Step 8, (b) step 28 and (c) step 32.

direction \mathbf{l}) and the kink (perpendicular to the slip direction so parallel to \mathbf{n}) directions respectively [28]. In order to determine the direction of the crack propagation, the value of D is plotted along these two directions for up to 4 μm from the crack tip, see Fig. 2b.

For the preset distance $R_0 = 2 \mu\text{m}$, the value of D along $\theta = 63^\circ$ is higher than along $\theta = 320^\circ$. Therefore, $\theta = 63^\circ$ is selected as the crack growth direction and this holds true all along the y -axis. As a side note, it was also found that for a mesh size chosen appropriately near the crack front, the crack growth direction does not depend on R_0 , at least for R_0 between 0.6 μm and 4 μm . The crack growth distance of 2 μm corresponds to approximately 3 elements of the FE mesh.

Fig. 4 shows intermediate stages (steps 8, 28 and 32) among the 32 steps of the crack propagation in the single slip single crystal [29]. It should be noted that at each step, 5 cycles are computed but each step may represent much more fatigue cycles depending on the chosen propagation distance or damage parameter threshold D_c . It can be observed that apart from a minor bifurcation along the kink direction, the crack propagated steadily in a rather constant direction close to $\theta = 60^\circ$. The short bifurcation occurred after 8 μm of crack propagation, i.e. 4 crack propagation events. This kind of crack bifurcation along the kink band direction does exist in fatigue experiments [28].

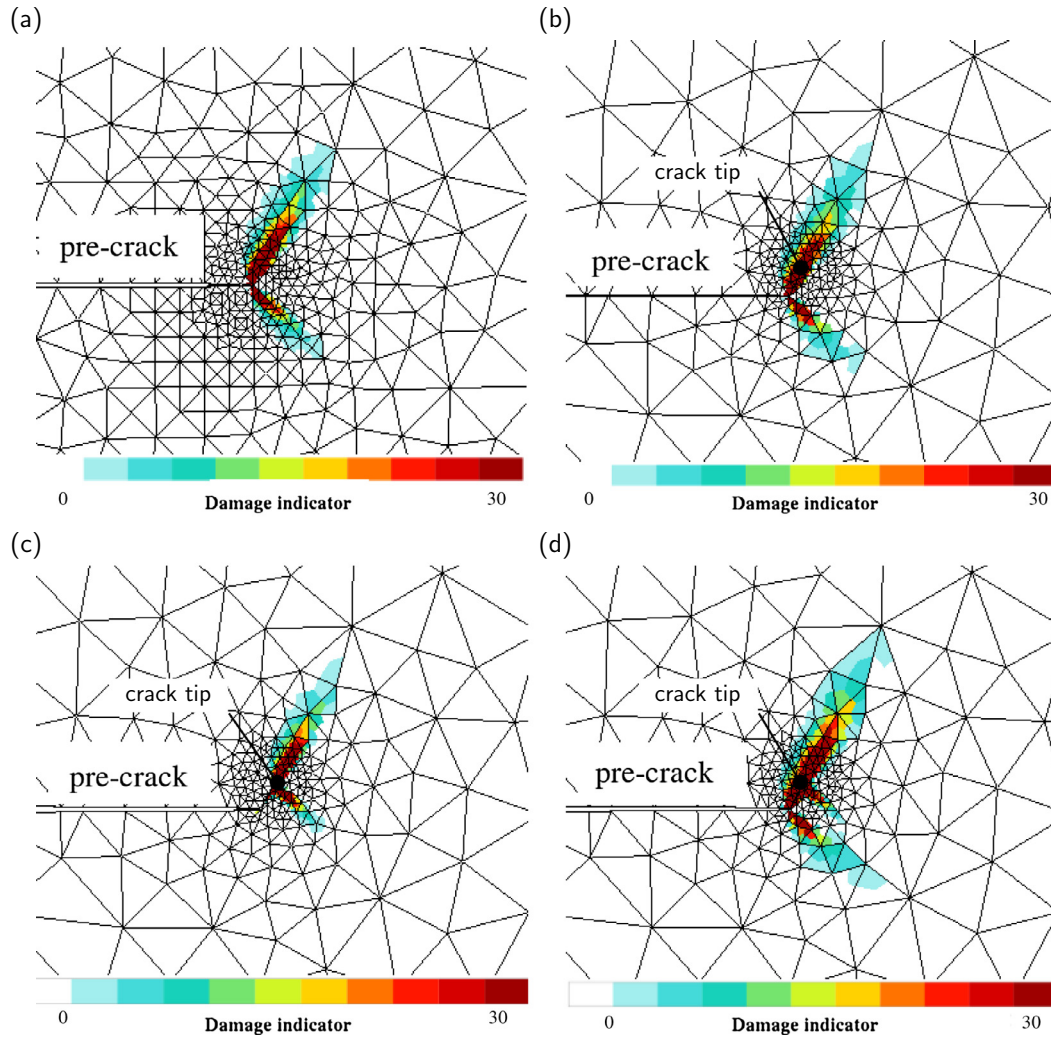


Fig. 5. Front view of the sample with damage indicator D (in MPa) at the crack tip (a) at the end of the first cycle, (b) at the beginning of the second cycle with transferred internal variables, (c) at the end of the second cycle without transferred internal variables, and (d) at the end of the second cycle with transferred internal variables.

In addition, it was found that the crack path is rather stable with respect to the parameter k (Eq. (5)). A second calculation with k set to zero was carried out and the crack path remains identical except that the crack bifurcation does not take place.

Apart from the small kink bifurcation event, the crack continues upwards, globally in the same direction as the first steps, until the crystal is completely broken. More precisely, as the crack moves forward the direction of crack propagation decreases progressively from $\theta = 63^\circ$ at the beginning to $\theta = 56^\circ$ due to the changing equilibrium of the structure and the free boundaries. It can be observed that the crack growth direction is not exactly parallel to the slip plane, oriented at an angle of $\theta = 54.7^\circ$ with respect to the horizontal direction. As a result, the crack surface does not exactly coincide with a definite crystallographic plane. The $\sim 10^\circ$ difference is consistent with a systematic study (not presented here) where the crystal is rotated with respect to the loading direction in a range $[0^\circ, 180^\circ]$. In each case, according to the maximum of D , the crack propagates in a direction close to the slip plane or the slip plane normal (they both play an equivalent mechanical role in the orientation tensor with the small strain formalism, see Eq. (3)). However, a systematic difference of about 10° between the crack growth direction and the slip plane or the slip plane normal is observed, which is attributed to the competition between crystal plasticity and the global mechanical equilibrium with the horizontal pre-crack. Another calculation with the pre-crack oriented

exactly parallel to the slip plane at $\theta = 54.7^\circ$ shows that the distribution of D is maximum at 54° , i.e. exactly along the crystallographic direction. This enforces the potential of our damage indicator D to properly describe the crystal plasticity based fatigue crack propagation at this scale.

3.3. Effect of the field transfer of state variables

Fig. 5a shows the damage indicator map at the end of the first cycle. Then, the crack was propagated by a distance of $2 \mu\text{m}$ along the direction $\theta = 63^\circ$ through remeshing. The new computation is initialised with the transferred variables, as shown in Fig. 5b. It can be observed that the extent of D around the crack tip is rather small with respect to the crack growth distance. Next, the computation continues and the distribution of D at the end of the second loading sequence is shown in Fig. 5d. Compared to the simulation without field transfer, in Fig. 5c, the interpolated value of D to the circles increases slightly in the direction of $\theta = 320^\circ$. However, the crack propagation direction remains the same at this step. This was expected due to the single slip system and the $2 \mu\text{m}$ propagation length, a distance where the accumulated plastic activity is rather small. Another comparison of the FE simulations with and without field transfer will be given in Section 4 for a single crystal with two slip systems.

4. Crack propagation in the case of two slip systems

In this section, the simulations of crack propagation in a single crystal with two slip systems, $(112)[11\bar{1}]$ and $(11\bar{2})[111]$, are presented. These two slip planes are symmetric with an angle of $\pm 54.7^\circ$ with respect to the pre-crack plane (perpendicular to U_z) and the slip directions are normal to the crack front $[\bar{1}10]$. The minimum element size at the crack tip is $0.1 \mu\text{m}$ and except for those elements, the simulation parameters remain identical to those presented in Section 3.

4.1. Propagation results

The first simulation is carried out without transferring state variables. The crack propagation distance is the same as in the

single slip case with $R_0 = 2 \mu\text{m}$. Applying the same boundary conditions as in Fig. 3, the results of 22 crack propagation steps are shown in Fig. 6a. Before the crack propagation, the value of $D = 18.5 \text{ MPa}$ along $\theta = 61^\circ$ is slightly higher than $D = 17.3 \text{ MPa}$ along $\theta = 299^\circ$. Therefore, the initial crack growth direction is selected along $\theta = 61^\circ$ with respect to the horizontal direction. The geometry, boundary conditions and slip systems are perfectly symmetric. The slight difference between the two slip systems activation therefore comes from small numerical discrepancies during the resolution, and interpolation of D within a non regular mesh (tetrahedron free meshing is used here). Once the crack started to propagate, the geometry is not symmetric any more.

Then, the CPFE continues and the value of D along the second slip system increases as imposed by the global mechanical equilibrium. The crack thus propagates along $\theta \sim 300^\circ$ for the second step. In this way, the crack grows alternatively along the two directions

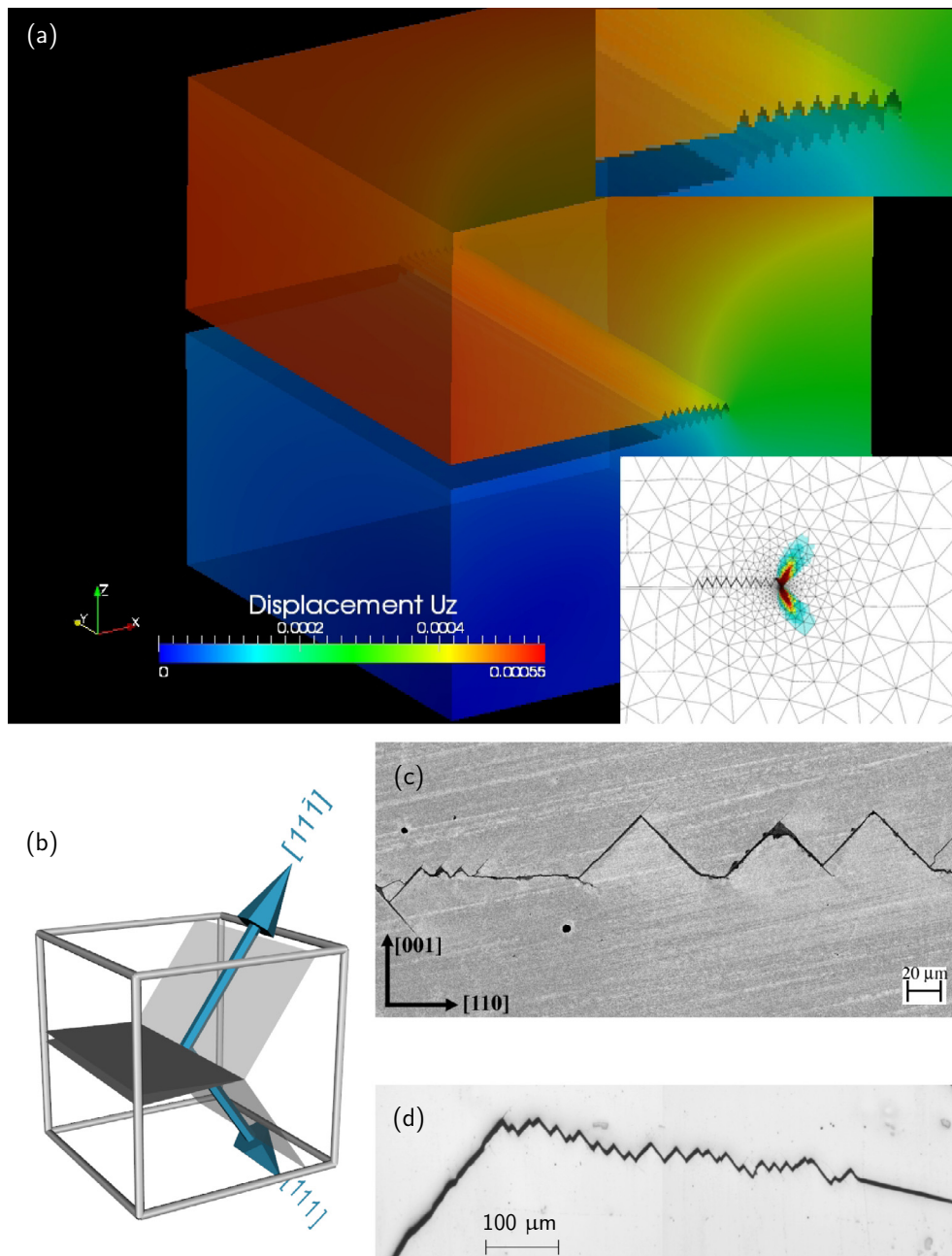


Fig. 6. (a) Simulation results of crack propagation in the double slip single crystal, (b) crystal geometry, (c) experimental crack bifurcation in a $(001)[110]$ nickel-based superalloy CT specimen in fatigue at 650°C [6], and (d) fatigue crack propagation in a Al-Cu-Mg alloy [10].

to form a zig-zag shape as shown in Fig. 6a. This type of crack bifurcation was observed in nickel-based superalloy at 650 °C as well as in a 2024 aluminium alloy, see Fig. 6b and c respectively. In each case, the particular crystallographic configuration is such that two slip systems equally activated are in competition.

Compared to the distribution of D in the single slip case (see for instance Fig. 2a), the maximum value of D in the double slip calculation is lower. This was expected since here two slip systems can accommodate the plastic strain at the crack tip. In a real situation, this would be associated to different values of the driving force for the crack (here modeled by D) which would lead to different crack growth rates.

It is important to note here that in this case, since the plastic fields are not transferred from one step to the next, the crack will bifurcate at each step whatever the propagation distance R_0 . Indeed, it appears that as soon as the crack grows into one direction, the mechanical equilibrium tends to promote the plastic activity in the other direction. This is confirmed by complementary simulations with the fixed crack growth distance set to 0.5 μm and to 1 μm . The crack bifurcates also after each loading sequence, leading to the same zigzag behaviour as in Fig. 6 but with a different crack path since the zigzag step corresponds to R_0 .

4.2. Effect of the field transfer of state variables

The second set of simulations takes into account the transferred field variables in order to compare the differences with the

previous calculations carried out with $R_0 = 0.5 \mu\text{m}$ and to determine where the crack will bifurcate. Fig. 7a and b shows the distributions of D at the end of the first propagation event. With the transferred variables, the accumulated values of D during the previous loading sequence are visible in the crack wake (see arrow on Fig. 7a). The crack propagates along the direction of $\theta = 59^\circ$. Fig. 7c shows the damage indicator after two crack propagation events. Because the variables are transferred from the previous step to the next, the value of D cumulates along the direction of $\theta = 59^\circ$ at each loading sequence. The systematic crack bifurcation did not occur at each step as without transferring the state variables. It can be anticipated that due to the increasing crack length, the mechanical equilibrium will change and at some point the crack bifurcation will take place, leading again to a zigzag pattern but independent of the value of R_0 this time.

5. Conclusive remarks

This work presented a new model to achieve crack propagation in a crystalline microstructure. The model is based on propagation through remeshing (the crack is explicitly introduced in the geometry as opposed to X-FEM methods) and the growth direction is evaluated thanks to a damage indicator D . This indicator is based on the accumulated plastic activity at the crack tip with a contribution of the shear and normal stresses acting on the glide planes. A short loading sequence is computed to assess the value of D along the crack front before the crack is propagated in three dimensions.

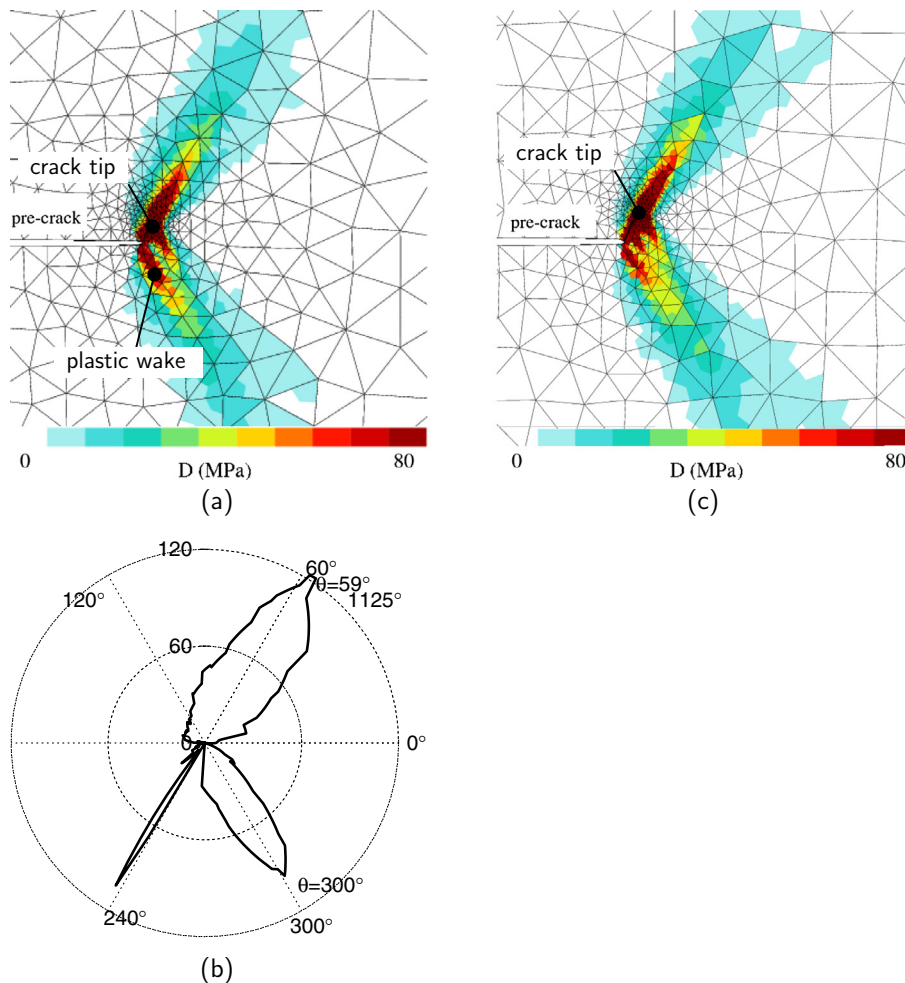


Fig. 7. Results with two slip systems and field transfer (a) at the end of the first propagation event (second loading sequence), (b) the corresponding value of D (in MPa) at a circle of $0.5 \mu\text{m}$ radius and (c) at the end of the second propagation event.

The method is also suitable to simulate the propagation in a polycrystal although only single crystals were used here for the sake of simplicity.

Two simplified examples were used to demonstrate the methodology. The propagation distance was set to a fixed value although it can also be inferred locally based on the distribution of D along the propagation direction. The predicted crack path appears stable with respect to mesh density and the choice of R_0 (the distance from the crack tip where to evaluate D). The loading sequence should be representative of the loading needed to establish the plastic quantities ahead of the crack tip, it may be one or more fatigue cycles. Ideally if the loading sequence is well chosen, running 10 propagation steps of $1\ \mu\text{m}$ would lead to the same result as 5 propagation steps of $2\ \mu\text{m}$. In the case of the single slip system, no qualitative difference between 1 and 5 cycles have been observed.

In Section 4, the crack propagation simulations of a single crystal with two slip systems were carried out. Without considering the field variables transfer, crack bifurcation occurred at the end of each loading sequence for the crack growth distance R_0 of $0.5\ \mu\text{m}$, $1\ \mu\text{m}$ and $2\ \mu\text{m}$. The zigzag crack propagation can be explained by the fact that the orientation of the slip systems is symmetric with respect to the pre-crack plane and the loading direction, which results in two symmetric branches with high values of D close to the two slip directions. As soon as the crack grows into one direction, the mechanical equilibrium tends to promote the plastic activity in the other direction so that the crack propagates along the two systems alternatively.

However, by conducting the calculations with field transfer, the crack bifurcation did not occur after two crack propagation steps for $R_0 = 0.5\ \mu\text{m}$. Because the $0.5\ \mu\text{m}$ crack growth distance is small compared to the plastic zone size, the plastic field of the previous step becomes important. It is clear that if the propagation distance is larger than the plastic zone size (the crack propagates to where D is zero), the plastic field transfer is not needed but the predicted crack path would be much less realistic. In addition, for future calculations with more realistic situations using a variable crack growth rate inferred by the choice of D_c , it is very likely that some part of the crack will propagate faster than others depending on the local crystallographic arrangement (this will be particularly true in polycrystals). In this case, the plastic wake effect will be more important at locations where crack propagation is slower. For instance it can be the case when stopped at a grain boundary where the values of D needs to cumulate to achieve the crack propagation. This emphasizes the importance of transferring the plastic fields when a very detailed description of the crack path is wanted.

Combined tomographic and diffraction observations of the 3D fatigue crack surface in [11] revealed that the crack propagates mostly on crystallographic planes, although a complex combination of slip planes is observed in each grain to achieve a more or less continuous crack. Since the present model is based on the crystal plasticity activity but does not strictly depend on crystallographic direction to select the crack propagation direction (values of D tend to grow higher in favourably oriented crystallographic directions but the global mechanical equilibrium also plays an important role), it may be well suited to reproduce at the mesoscale the complex crack path observed in the first few grains. Calculations using realistic polycrystalline samples such as shown in [11] are under way to test the model capabilities further.

Acknowledgement

This work was carried out under the French ANR Project CRYSTAL 2010-BLAN-91801.

References

- [1] Forsyth PJE. Fatigue damage and crack growth in aluminium alloys. *Acta Metall* 1963;11:703–15.
- [2] Bilby BA, Cottrell AH, Swinden KH. The spread of plastic yield from a notch. *Proc R Soc A* 1963;272:304–14.
- [3] Tanaka K, Akiwari Y, Nakai Y, Wei RP. Modelling of small fatigue crack growth interacting with grain boundary. *Eng Fract Mech* 1986;24:803–19.
- [4] Neumann P. Coarse slip model of fatigue. *Acta Metall* 1969;17:1219–25.
- [5] Suresh S. *Fatigue of materials*. 2nd ed. Cambridge University Press; 1998.
- [6] Marchal N. Propagation de fissure en fatigue-fluage haute température de superalliages monocristallins base de nickel. PhD thesis, ENSMP; 2006.
- [7] Ignatiev KI, Lee W-K, Fezzaa K, Stock SR. Phase contrast stereometry: fatigue crack mapping in three dimensions. *Philos Mag* 2005;85(28/1):3273–300.
- [8] Khor KH, Buffière J-Y, Ludwig W, Sinclair I. High resolution X-ray tomography of micromechanisms of fatigue crack closure. *Scr Mater* 2006;55(1):47–50.
- [9] Buffière JY, Ferrière E, Proudhon H, Ludwig W. 3D visualisation of fatigue cracks in metals using high resolution synchrotron. *Mater Sci Technol* 2006;22(9):1019–24.
- [10] Proudhon H, Moffat A, Sinclair I, Buffière J-Y. Three-dimensional characterisation and modelling of small fatigue corner cracks in high strength Al-alloys. *CR Phys April* 2012;13(3):316–27.
- [11] Herbig M, King A, Reischig P, Proudhon H, Lauridsen EM, Marrow J, Buffière J-Y, Ludwig W. 3-D growth of a short fatigue crack within a polycrystalline microstructure studied using combined diffraction and phase-contrast X-ray tomography. *Acta Mater* 2011;59:590–601.
- [12] Ludwig W, King A, Herbig M, Reischig P, Marrow J, Babout L, et al. Characterization of polycrystalline materials using synchrotron X-ray imaging and diffraction techniques. *JOM* 2010;62:22–8.
- [13] Schaefer W, Marx M, Vehoff H, Heckl A, Randelzhofer P. A 3-D view on the mechanisms of short fatigue cracks interacting with grain boundaries. *Acta Metall* 2011;59:1849–61.
- [14] Asaro RJ. Crystal plasticity. *J Appl Mech* 1983;50:921–34.
- [15] Méric L, Poubanne P, Cailletaud G. Single crystal modeling for structural calculations: Part 1 – Model presentation. *J Eng Mater Technol* 1991;113:162–70.
- [16] Rice JR. Tensile crack tip fields in elastic-ideally plastic crystals. *Mech Mater* 1987;6:317–35.
- [17] Aslan O, Forest S. Crack growth modelling in single crystals based on higher order continua. *Comput Mater Sci* 2009;45:756–61.
- [18] Castelluccio Gustavo M, Musinski William D, McDowell David L. Recent developments in assessing microstructure-sensitive early stage fatigue of polycrystals. *Curr Opin Solid State Mater Sci* 2014;18(4):180–7. Slip Localization and Transfer in Deformation and Fatigue of Polycrystals.
- [19] Vattré A, Devincre B, Roos A. Orientation dependence of plastic deformation in nickel-based single crystal superalloys: discrete–continuous model simulations. *Acta Mater* 2010;58:1938–51.
- [20] Prasad Reddy GV, Robertson C, Depres C, Fivel M. Effect of grain disorientation on early fatigue crack propagation in face-centred-cubic polycrystals: a three-dimensional dislocation dynamics investigation. *Acta Mater* 2013;61:5300–10.
- [21] A non-linear material & structure finite elements software suite Z-set. <<http://www.zset-software.com>>, version 8.5.
- [22] Cheng A, Laird C. The transition from stage I to stage II fatigue crack propagation in copper single crystals cycled at constant strain amplitudes. *Mater Sci Eng* 1983;60:177–83.
- [23] Fatemi A, Socie DF. A critical plane approach to multiaxial fatigue damage including out-of-phase loading. *Fatigue Fract Eng Mater Struct* 1988;11:149–65.
- [24] Dang Van K, Cailletaud G, Flavenot JF, Le Douaron A, Lieurade HP. Criterion for high cycle fatigue failure under multiaxial loading. In: Brown MW, Miller KJ, editors. *Biaxial and multiaxial fatigue*. London, UK: Mechanical Engineering Publications; 1989. p. 459–78.
- [25] Hochhalter JD, Littlewood DJ, Christ Jr RJ, Veilleux MG, Bozek JE, Ingraffea AR, et al. A geometric approach to modeling microstructurally small fatigue crack formation: II. Physically based modeling of microstructure-dependent slip localization and actuation of the crack nucleation mechanism in AA 7075-T651. *Model Simul Mater Sci Eng* 2010;18:045004.
- [26] Chiaruttini V, Geoffroy D, Riolo V, Bonnet M. An adaptive algorithm for cohesive zone model and arbitrary crack propagation. *Eur J Comput Mech* 2012;21:208–18.
- [27] Chiaruttini V, Riolo V, Feyel F. Advanced remeshing techniques for complex 3D crack propagation. In: 13th International conference on fracture. Beijing, China; 2013.
- [28] Flouriot S, Forest S, Rémy L. Strain localization phenomena under cyclic loading: application to fatigue of single crystals. *Comput Mater Sci* 2003;26:61–70.
- [29] Li J, Proudhon H, Roos A, Chiaruttini V, Forest S. Crystal plasticity finite element simulation of crack growth in single crystals. *Comput Mater Sci* 2014;94:191–7.